

Decoding Gray Matter: large-scale analysis of brain cell morphometry to inform microstructural modeling of diffusion MR signals

Charlie Aird-Rossiter^{1,2,*}, Hui Zhang³, Daniel C. Alexander³,
Derek K. Jones¹, and Marco Palombo^{1,2,*}

¹*Cardiff University Brain Research Imaging Centre (CUBRIC), School of Psychology, Cardiff University, Cardiff, United Kingdom*

²*School of Computer Science and Informatics, Cardiff University, Cardiff, United Kingdom*

³*UCL Hawkes Institute and Department of Computer Science, University College London, London, United Kingdom*

**Corresponding authors: Charlie Aird-Rossiter, aird-rossiterc@cardiff.ac.uk and Marco Palombo, palombom@cardiff.ac.uk*

Abstract

Diffusion-weighted MRI (dMRI) is a formidable technique for non-invasively characterizing brain microstructure. Biophysical modelling is often necessary to gain specificity to cellular structure.

However, designing sensible biophysical models and appropriate dMRI acquisitions is challenging, especially for gray matter (GM), as little is known about typical values of relevant features of braincell morphology contributing to dMRI signal. This work addresses this unmet need: We analysed about 3,500 cells from mouse, rat, monkey and human brains to determine statistical distributions of a set of morphological features (structural, topological and shape descriptors) relevant to GM microstructure modelling.

Illustrative examples demonstrate how this study can inform biophysical modelling and important implications for biophysical modelling of GM are discussed, enabling the design of more sensible models and suitable data acquisitions.

1 Introduction

Grey matter (GM) is composed of a range of cells, mainly differentiated into neuronal and glial cells, featuring a plethora of morphological characteristics. Neurons are fundamental functional units of the nervous system, specialized in

the transmission and integration of electrical and chemical signals within the brain. Supporting the neurons are the glial cells (e.g. astrocytes, microglia and oligodendrocytes) that are crucial in maintaining the health and functionality of neurons.

First studied in depth by Ramon y Cajal in the late 19th century [1], neuronal morphology offers insights into the complex structure and function of the brain. Neurons come in various shapes and sizes, tailored for their respective functions [2]. Neurons can be classified according to their morphological, molecular, and physiological characteristics [3]. Both neurons and glia have similar structures, both having a central cell body (or soma) and branching projections, and show remarkable diversity and variability depending on the brain region [4, 5], e.g., from the complex branching patterns of Purkinje cells in the cerebellum to the more simple granule cells of the cerebral cortex.

The brain contains about 86 billion neural¹ cells [6]. Cortical GM is roughly constituted of 10–40% cell bodies (soma) of neural cells; 40–75% neurites: neuronal dendrites, short-range intra-cortical axons, the stems of long-range axons extending into the WM and glial cell projections which intermingle with each other to form a dense and complex network; 15–30% highly tortuous extracellular space (ECS); and 1–5% vasculature [7, 8, 9]. In adults, the glia to neuron ratio is 1.32/1.40 for males/females respectively. The proportion of glial cells (by cell count) was estimated to be 77% oligodendrocytes, 17% astrocytes and 6% microglia [10, 11].

The ECS occupies a volume fraction of 15–30% in normal adult brain tissue, with a typical value of 20%, that falls to 5% during global ischemia (the expected state during classical fixation) [12]. The ECS has an average tortuosity (defined as the ratio between the true diffusion coefficient and the effective diffusivity of small molecules such as inulin and sucrose) of 2–3 [12], due to its labyrinthine porous matrix, the presence of long-chain macromolecules, transient trapping in dead-space microdomains, and transient physical-chemical interaction with the cellular membranes. The width of the ECS of the brain cortex is 40–120 nm [13], although this is less established because chemicals used in the processing of the tissue for the display introduce shrinkage effects that can range from 1–65% [14]. The average neuron-microvessel distance in brain GM is 20 μm [15].

The morphology of neurons and glia is revealed through staining and microscopy techniques such as confocal or electron microscopy [16, 17, 18], which can image cellular structures with very high resolution (down to a few nanometers) [19]. However, currently there are no means to directly observe the cellular microstructure in vivo and without invasively using imaging techniques, such as Magnetic Resonance Imaging (MRI), as the cellular scale (on micrometers) lies beyond the resolution of clinical MRI, generally on the mm scale [20]. With many neurological conditions, including aging [21], altering the brain structure on this cellular scale, there is a strong incentive to develop means of revealing

¹neural should not be confused with neuronal. Neural means relating to the nervous system (hence referring to any cell type in the brain: from neurons to glia), while neuronal means relating to neurons.

the morphology of neural cells, in-vivo.

Given its sensitivity to the micrometer length scale, diffusion-weighted MRI (dMRI) is a promising technique to address the resolution limit of MRI and characterize the brain structure in vivo at the cellular scale, that is, the *microstructure*. However, this sensitivity is indirect and biophysical modelling of the dMRI signal in the brain tissue is essential to quantify histologically meaningful features of the cellular structure and gain specificity to their changes. To this end, the *microstructure imaging* paradigm has been introduced over a decade ago [14]: the approach voxel-wise fits a biophysical model to the set of signals obtained from images acquired with different sensitivities, yielding model parameter maps proxy of the corresponding microstructural features.

Successful examples of the microstructure imaging paradigm include Diffusion Tensor Imaging (DTI) [22], the Neurite Orientation Dispersion and Density Imaging (NODDI) [23] and the White Matter Tract Integrity (WMTI) [24] to characterise the diffusion of water within white matter (WM), revealing insight into the structure of axonal bundle tracks and other anatomical features, such as axon diameter [25, 26], opening new and exciting opportunities in the field of neuroscience.

Following the success of dMRI in WM, there has been a significant increase in interest in its application in GM, with the hopes of characterizing the cellular morphology within the brain in vivo. So far, dMRI has been used to differentiate different areas of cortical grey matter and reveal laminar structure within grey matter [27]. Great effort has been made to develop also models to better describe the diffusion signal within GM and reveal anatomical information about the microstructure, such as the Soma And Neurite Density Imaging (SANDI) [28] to characterize soma and neurite density, the Neurite EXchange Imaging (NEXI) [29] and the Standard Mmodel with EXchange (SMEX) [30] to characterize the water permeative exchange between neurites and extracellular space, and combinations of these, such as SANDI with exchange (SANDIx) [30].

While substantial effort has been made to design, validate, and translate to clinics biophysical models for WM microstructure imaging [14, 31, 32], the GM counterpart is lagging. This is due to the greater complexity of the tissue, which renders the design of biophysical models for GM microstructure imaging more challenging [33].

To design sensible biophysical models and appropriate dMRI acquisitions for GM, it is critical to identify which relevant microstructural features of the complex GM tissue can be measured, how they can be estimated accurately and how such estimates can be validated. It is also very helpful to identify the typical values of such relevant features. With cellular morphology varying by cell type as well as brain region, there is a necessity for a thorough analysis of characteristics based on these criteria. Whilst substantial effort has been put towards the fine characterisation of WM axonal morphology there is yet to be the same level of in-depth analysis dedicated to GM cellular morphology.

Here we aim to correct this imbalance with a comprehensive analysis of GM cellular morphology, looking at structural and topological morphology, and shape descriptors of over 3,500 real three-dimensional reconstructions from

mouse, rat, monkey, and human brain cortex.

The paper is organized as following. We first provide quantitative information on the anatomy of brain GM tissue at the cellular scale, which is the primary target for microstructure imaging through dMRI. We characterize the morphology of neural cells using structural, topological and shape descriptors. We then review the range of dMRI measurements and biophysical models available to probe this anatomy and highlight limitations and caveats, ultimately providing guidelines on how to model dMRI signals in GM.

2 Methods

2.1 Microscopy Dataset

In order to measure characteristic features for specific cell types, the open access repository Neuromorpho.org [34] was used, for comprehensive range of cellular reconstructions available. We downloaded and analysed three dimensional reconstructions of 3,598 brain cells, from mouse, rat, monkey, and human, in the form of SWC files. The "SWC" encodes for the last names of its initial designers Ed Stockley, Howard Wheal, and Robert Cannon and is an ASCII text-based file that describes three-dimensional neuronal or glial morphology. The SWC file defines a set of labelled nodes connected by edges characterizing the three-dimensional structure of each cell Fig.1.

The cells acquired were representative of eight cell types: microglia, astrocyte, pyramidal, granule, purkinje, glutamatergic, gabaergic, and basket cells, from mouse/rat (N=1,358), monkey (N=948), and human (N=1,292). Although the NeuroMorpho database contains over 270,000 cellular reconstructions, only 4,278 satisfied our inclusion criteria: healthy controls; having complete reconstruction of all the dendrites; containing full information about diameters and angles; and being three-dimensional reconstructions. Of these, 680 did not pass our visual inspection on the quality of the reconstruction and were excluded. Our quality assessment criteria include: consistent estimates of dendritic diameters (e.g., most of the 680 reconstructions had a fixed nominal diameter for all the branches instead of the real one); continuity of the cellular processes; minimal reconstruction artifacts (e.g., most of the 680 reconstructions had artifactual shrinkage in the Z direction).

To reveal the skeletal structure of the cells, dendritic spines (small protrusions situated on neuronal dendrites, providing synaptic connections) were not included in the cellular reconstructions analysed to avoid them to bias the statistics of the overall cellular morphology, e.g. drastically shortening the branch length and increasing the branch order.

The cellular reconstructions were analysed in matlab (Mathsworks) using custom scripts, exploiting functions from validated suites (TREES [35], Blender [36], ToolboxGraph [37]). All the codes and SWC files used in this work will be made publicly available on GitHub upon publication.

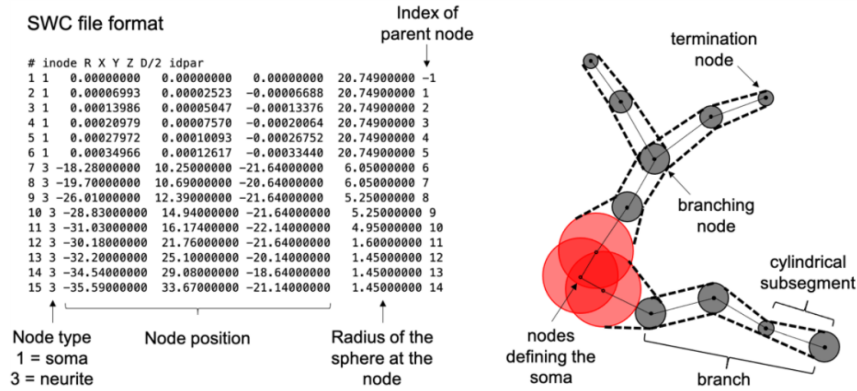


Figure 1: **An example of SWC file and how it relates to the cellular geometry.** We highlight the structural elements used to estimate the morphological features. Note that the first node in the SWC file is the so called ‘root’. It often coincides with the soma’s centre and it is used to compute metrics.

2.2 Structural descriptors

The structural analysis describes the constituent parts of the cell, providing information about the general properties of the cell, the soma and the cellular projections. These features provide vital information about the fundamental skeleton of the cell such as effective soma radius and the branch angle formed between two daughter branches.

For the structural analysis, features or descriptors, determined to be crucial to microstructure modelling based on current literature [38, 28, 39, 40, 41, 42, 43, 44, 45, 46, 47], were estimated from the real data. This set of features enables us to understand better how each basic constituent of the brain cell morphology can impact the diffusion of molecules within the intra-cellular space. For example, the size of the soma and the cellular projections can inform on the characteristic length scales of intra-cellular restrictions; cellular projections’ branching, tortuosity, undulation and calibre coefficient of variation can inform on time dependence, and the soma and projections surface-to-volume ratios can inform on exchange.

The features of the soma and cellular projections are very different, so our analysis reflects that by dividing the structural descriptors into appropriate categories. These categories are: *soma* (the characteristics defining the cell body), *projections* (the set of characteristics defining the cellular projections’ structure as interconnected branches) and *general* (describing the general cellular characteristics).

Soma

- R_{soma} : the effective radius of the soma

- η_{soma} : the proportion of the surface area covered by projection interfaces
- S/V_{soma} : the soma surface to volume ratio

Projections

- $\langle R_{branch} \rangle_s$: the mean effective radius of segments along branch s
- CV_{branch} : a measure of branch beading
- L_{branch} : the branch length
- S/V_{branch} : the branch surface to volume ratio
- $\langle \mu OD_{branch} \rangle_s$: a measure of mean branch undulation
- $\langle R_c \rangle_s$: a measure mean branch curvature
- τ_{branch} : a measure of branch tortuosity
- θ_{branch} : the angle formed by two bifurcating branches

General

- R_{domain} : the extent of the cellular domain
- $N_{projection}$: the number of primary projections radiating from the soma
- BO : the degree of branching of the cellular projections

An illustration of the structural descriptors investigated is reported in Fig.2 and a summary of their definitions is reported in Tab.1.

From the information in the cellular reconstruction SWC file, the nodes/edges defining the projections from those belonging to the soma were separated: all the nodes and corresponding edges within a distance 1.5x the nominal soma radius (radius of the first node in the SWC file) from the first node, namely the 'root', were assigned to the soma; the remaining ones to the projections.

Using this soma threshold the cell was resampled, preserving the nodes that lie within the soma threshold. From this resampled soma the 3D surface mesh was constructed using Blender and the volume, V_{soma} , and surface, S_{soma} , of the soma calculated. The soma volume can be expressed in terms of the effective soma radius R_{soma} , which is the radius of a sphere of equivalent volume. Additionally, we calculated also the soma surface-to-volume ratio, S/V_{soma} as ratio between S_{soma} and V_{soma} ; and the fraction of the soma surface covered by the cellular projections as sum of the projection connection area divided by the soma surface area (η_{soma}).

From the nodes/edges defining the projections, the individual branches composing the cellular projections were identified, delimited by either branching or termination nodes. The individual branches are comprised of cylindrical sub-segments, defined by the edges and their associated radius. The central line defined by these sub-segments gives a curvilinear path, s . From this path, s ,

Morphological feature	Definition
R_{soma}	Radius of sphere of volume equivalent to the soma surface volume
$\langle R_{branch} \rangle_s (\langle R_{branch}^2 \rangle_s)^{1/2}$	Mean (standard deviation) of subsegments' radius along s
CV_{branch}	Coefficient of variation of radius
L_{branch}	Sum of subsegments' length in s
S/Z_{branch}	Ratio between the sum of the surfaces of all the subsegments in s and the sum of their volume
$\langle \mu OD_{branch} \rangle_s$	Mean microscopic orientation dispersion
$\langle R_c \rangle_s$	Mean radius of curvature of s
τ_{branch}	Ratio between distance between ends of s and L_{branch} , branch tortuosity is τ_{branch}^{-1}
BO	The number of consecutive bifurcations of the cellular projections
N_{proj}	The number of primary projections radiating from the soma
η_{soma}	Ratio between the total cross-sectional area of the N_{proj} primary projections and the total surface area
R_{domain}	Distance of the furthest node from the soma

Table 1: **Definition of the structural descriptors investigated.**

metrics for the projections features were computed. Branch beading is reported as the coefficient of variation of the branch radius along the branch length (CV_{branch}). The branch surface-to-volume ratio (S/V_{branch}) was determined as the sum of the sub-segments area divided by the sum of the sub-segments volume. Branch undulation ($\langle \mu OD_{branch} \rangle_s$) is calculated as the mean angle made by the vector of the individual sub-segments and the vector made by the branch start and end points.

Finally, the general metrics were computed. The cellular domain R_{domain} is defined as the maximum Euclidean distance from the root presented in each cell. The number of projections $N_{projection}$ was found by identifying the number of branches that cross the soma threshold. And the branch order BO is defined as the number of consecutive bifurcations of the cellular projections.

We believe these characteristics can be used to model GM cells [47] and inform dMRI sequence design to maximise acquisition sensitivity to cellular features.

We provide the mean and standard deviation for each structural descriptor for each cell type for each species analysed. Moreover, we also provide value distributions for features of relevance to biophysical modelling of diffusion in GM, such as R_{soma} ; L_{branch} and estimated intracellular residence times based on the surface-to-volume ratio of the whole cell: S/V_{domain} and the individual branches: S/V_{branch} .

2.3 Shape descriptors

Many diffusion models of the diffusion MRI signal rely on modelling the cellular structure as a collection of randomly orientated cylinders in space [23, 51]. Whilst this was initially applied to modelling the signal from white matter where axons can be simplified to a collection of cylinders/sticks this model has been shown to apply to the dendrites of neurons [28, 29] and has been incorporated into current grey matter models of the diffusion signal. The cellular structure is modeled as a collection of cylinders, enabling the computation of fractional anisotropy (FA).

To calculate FA we followed the method outlined in [40]. This involves decomposing the cell into its primary projections and further segmenting these

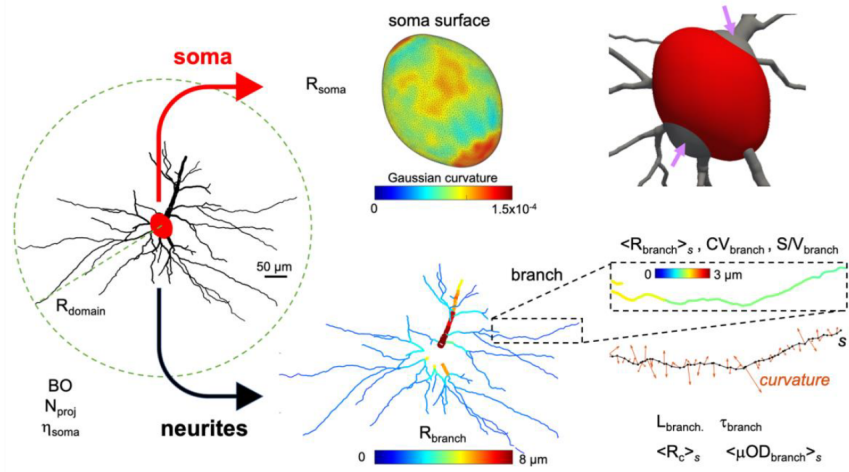


Figure 2: **Illustration of the structural descriptors investigated for an exemplar cell.** We estimated general features of the whole structure and separated soma from projections, processing them individually to estimate a set of other relevant features. Additionally, we display the Gaussian curvature of the soma surface to show that it is a non-spherical geometry (always positive but not constant). A limitation of the current approach (and the majority of existing tools [48, 49, 50]) is the slightly inaccurate definition of the soma surface, as shown in the top right corner (arrows).

into cylinders of length $l = 10\mu m$. From these segments the FA can be calculated by first computing the scatter matrix of the weighted line segments (weighted by their volume), from which the eigenvalues (τ_i) can be found (Fig.3). The FA can be calculated from these eigenvalues using the following equation.

$$FA = \sqrt{\frac{3}{2} \frac{(\tau_1 - \tau)^2 + (\tau_2 - \tau)^2 + (\tau_3 - \tau)^2}{\tau_1^2 + \tau_2^2 + \tau_3^2}}$$

It should be noted, due to the limited depth of field of some of the cellular reconstructions due to the method of acquisition, some cells appear flattened in dimension the perpendicular to the plane of the acquisition, which would result in an artificially high FA. To account for this, assuming that cells are axially symmetric, if the first eigenvalue was significantly lower than the second, $\tau_1 \ll \tau_2$, then the first eigenvalue was set to equal second, $\tau_1 = \tau_2$, and all eigenvalues were normalized such that, $\sum_{i=1}^3 \tau_i = 1$.

The FA was calculated for all cells and the mean and standard deviation are reported.

In addition to the FA of the line segments, their orientation dispersion (OD) was also computed. OD provides additional insight into the degree of anisotropy in cellular structures, complementing FA by describing the variability in the

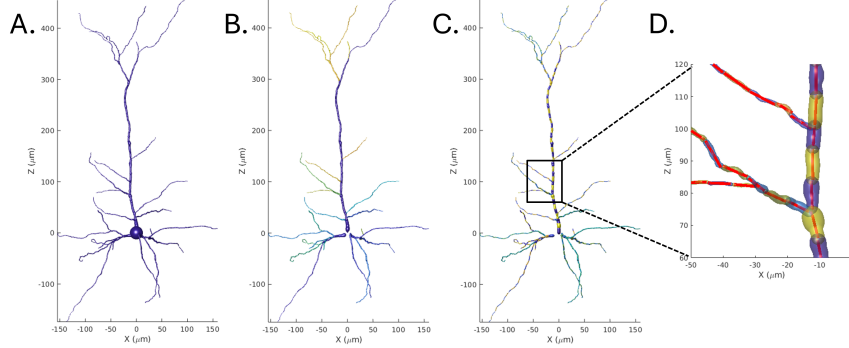


Figure 3: **A demonstration of procedure used to decompose the cellular structure into a set of average line segments.** A. the complete cell. B. cell decomposed into topological persistence components. C. cell further decomposed into 10 μm segments. D. average line segments fitted to cell segments.

directions of the neuronal projections. The variability is typically characterised through a Watson distribution, which is a probability distribution of orientations around the primary axis on the unit sphere [52]. With the degree of clustering defined by the concentration parameter, κ . This concentration parameter can be used to calculate the OD through the following equation [23].

$$OD = \frac{2}{\pi} \arctan(1/\kappa)$$

For cases where the data is not axially symmetric, such as cellular reconstructions with limited depth, the Watson distribution is insufficient as the orientation data is highly anisotropic. Instead, we applied the more general Bingham distribution, which accounts for orientation variability along multiple axes. The Bingham distribution models anisotropic orientation data and provides two concentration parameters (κ_1 and κ_2), corresponding to the clustering along two orthogonal directions/planes.

To account for this variability in the cellular reconstructions a Bingham distribution was fitted to the weighted line segments using the MATLAB tool box libDirectional [53] (Fig.4). From the resulting concentration parameters, if the first concentration parameter was significantly larger than the second $\kappa_1 \gg \kappa_2$, indicating the orientation data was highly planar, κ_2 was used as the Watson distribution parameter κ . Otherwise, the average of κ_1 and κ_2 was used as the Watson distribution parameter κ .

This approach provides a robust calculation of the Watson distribution across isotropically and anisotropically orientated data sets

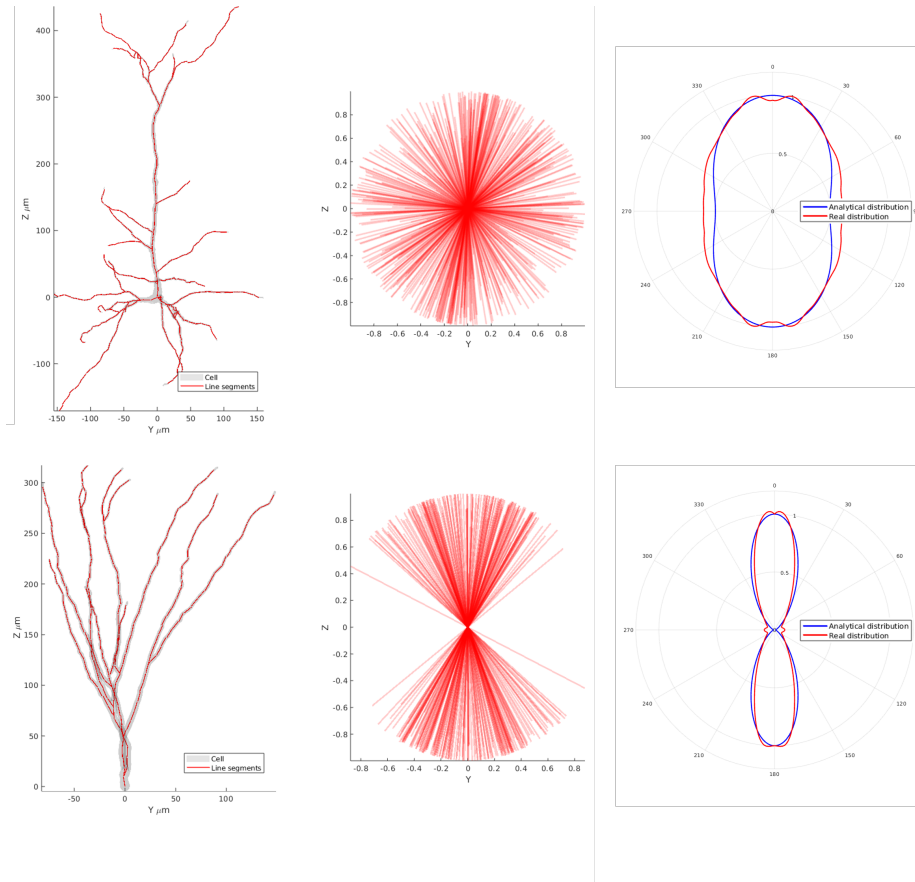


Figure 4: **A comparison between two cell types, mouse/rat pyramidal and granule cells.** Showing exemplar cells over layed with decomposed line segments, the line segments centered at the origin, and orientation distribution about the z axis of the line segments and the analytical distribution given the calculated Watson concentration parameter

2.4 Topological descriptors

Another way of characterising cells is to look at their topology, which can provide a valuable means of characterising their complex branching structures. One such characterisation is the Topological Morphology Descriptor (TMD) [54]. The TMD returns the topological persistence barcode of the given structure. This barcode concisely encodes the branching structure of the cell, and has been shown to be highly effective in the generation of synthetic neurons [55]. Here, we apply the TMD to characterize the cellular projections and compare cellular topology across cell-types and species.

Topological persistence analyses at what length scales a given topological

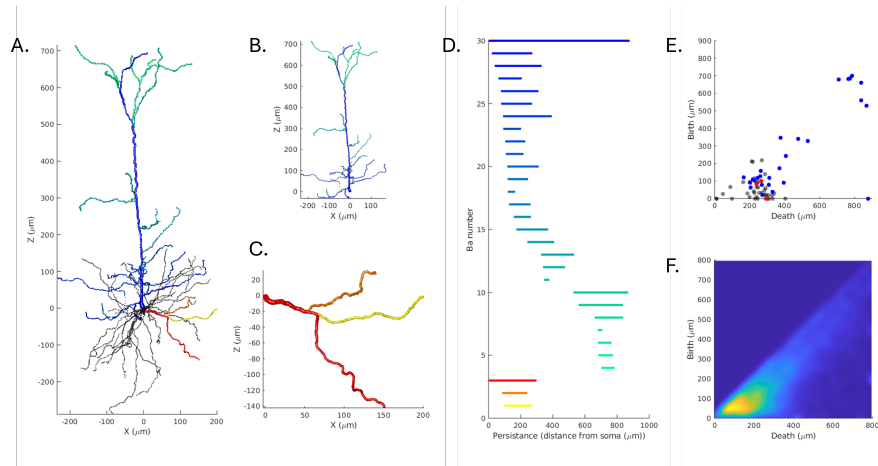


Figure 5: **A representation of the process of decomposing a cellular structure** (here a mouse/rat pyramidal cell) into its corresponding topological persistence bar code for an apical and basal projection. A. The complete cellular structure of an exemplar cell, apical projection in blue, and exemplar basal projection in red. B. and C. Detail of apical and basal projections being assessed. D. Corresponding barcodes for apical (in blue) and exemplar basal (in red/orange) components. E. persistence diagram of the complete cell, (blue points corresponding to apical and red points to the exemplar basal projection, black points for the remaining projections). F. The resulting persistence image for all mouse/rat pyramidal cells.

feature, here the path length of connected branches, persists. The TMD is computed by tracking the initiation points and termination points, with respect to path length from the soma, of the connected branches at different length scales [56], preserving the longer components and filtering out the shorter ones. This is computed over the individual neurite projections, not the entire cell.

The terminal branches are evaluated with respect to their path length from the soma. Branches that share a parent node are compared and the branch with the shorter path length is filtered and its initiation length (path length of the parent node) and termination length are recorded. The longer branch is preserved and the process is repeated for all remaining branches, until there is only one remaining branch that corresponds to the path from the soma to the terminal point with the greatest path length. The returned barcode is a multi set of pairs of numbers, describing the initiation and termination of each constituent bar in the neurite, with respect to the path distance from the soma. The topological barcode has been shown to retain detailed information of the structure it was computed for and can be used to categorise and identify cell types [55].

In this work the cells were first decomposed into their principle projections,

by identifying the projections originating from the soma, and persistence barcodes from these projections were identified. The identified barcodes were used to create persistence images for each cell type (Fig.5). These images visualize the persistence of components based on their birth and death lengths. To enhance smoothness, Gaussian smoothing was applied, and the images were normalized so that the sum of their entries equaled one

Comparisons were made between persistence images by computing the global topological distance, D , between images,

$$D = \frac{\sum_{i=1}^n |Im1_i - Im2_i|}{n}$$

This topological distance was calculated for cell types within species and also cell types between species.

3 Results

3.1 Morphological features' reference values

A summary of the structural features typical values can be seen in Tab.2. Some features show little variation between cell type and species ($\langle R_{branch} \rangle_s$, CV_{branch} , $\langle \mu OD_{branch} \rangle_s$, and τ_{branch}). The remaining features displayed a wide range of values, suggesting higher inter-cellular and intra-species variability.

3.2 Comparing neuronal and glial cells

Given the growing interest in differentiating neurons and glial cells, the mean values of the structural features were computed across only neuronal and glial cells and reported in Tab.3. The findings show, compared to glial cells, neurons had larger soma and cell domain and longer branches; and reduced branching, branch curvedness, number of primary projections, and proportion of soma surface covered by projections; the remaining features displayed similar values.

3.3 Cellular shape reference values

A summary of the shape descriptors typical values for each cell type and species are reported in Tab.4. Cells with highly oriented and polarized projections, such as Purkinje cells, granule cells and pyramidal neurons have high FA and low orientation dispersion; while most of the glial cells projections are highly dispersed and with low FA.

Cell Type	Species	N	$R_{\text{dendrite}}(\mu\text{m})$	N_{proj}	BO	S/V_{dendrite}	$R_{\text{ soma}}(\mu\text{m})$	$\eta_{\text{ soma}}(\%)$	$S/V_{\text{ soma}}(\mu\text{m}^{-1})$	$S/V_{\text{ soma}}(\mu\text{m}^{-1})$	$L_{\text{branch}}(\mu\text{m})$	$R_{\text{branch}}(\mu\text{m})$	CV_{branch}	μOD_{branch}	$R_c(\mu\text{m})$	τ_{branch}
Microglia	mouse/rat	169(123)	62 ± 70	9 ± 3	9 ± 4	2.5 ± 1.1	≥ 4.7 ± 6.3	≤ 4.7 ± 2.9	0.52 ± 0.38	4.3 ± 1.6	20 ± 13	≥ 2.1 ± 2.5	0.95	0.26 ± 0.05	≥ 34 ± 31	0.89 ± 0.03
	monkey	61(60)	42 ± 8	8 ± 2	10 ± 4	5.2 ± 1.1	2.73 ± 0.50	≤ 1.4 ± 1.1	1.0 ± 0.25	16 ± 2	7.2 ± 5.7	≥ 6.0 ± 0.29	1.2	0.30 ± 0.04	0.91 ± 0.02	0.91 ± 0.02
	human	n.a.	n.a.	n.a.	n.a.	n.a.	n.a.	n.a.	n.a.	n.a.	n.a.	n.a.	n.a.	n.a.	n.a.	n.a.
Astrocyte	mouse/rat	269(247)	40 ± 14	11 ± 7	19 ± 8	2.3 ± 0.65	≥ 2.1 ± 0.96	≤ 8.6 ± 2.6	0.88 ± 0.37	6.3 ± 2.2	4.9 ± 2.6	≥ 2.4 ± 1.0	0.55	0.26 ± 0.05	≥ 3.5 ± 1.2	0.88 ± 0.03
	monkey	n.a.	n.a.	n.a.	n.a.	n.a.	n.a.	n.a.	n.a.	n.a.	n.a.	n.a.	n.a.	n.a.	n.a.	n.a.
	human	n.a.	n.a.	n.a.	n.a.	n.a.	n.a.	n.a.	n.a.	n.a.	n.a.	n.a.	n.a.	n.a.	n.a.	n.a.
Oligodendrocyte	mouse/rat	80(80)	71 ± 19	15 ± 5	10 ± 3	0.67 ± 0.24	≥ 8.9 ± 1.7	≤ 61 ± 2.0	0.35 ± 0.06	13 ± 0.1	12.4 ± 3.4	≥ 0.3 ± 0.0	0.62	0.16 ± 0.02	10 ± 1.1	0.81 ± 0.05
	monkey	n.a.	n.a.	n.a.	n.a.	n.a.	n.a.	n.a.	n.a.	n.a.	n.a.	n.a.	n.a.	n.a.	n.a.	n.a.
	human	n.a.	n.a.	n.a.	n.a.	n.a.	n.a.	n.a.	n.a.	n.a.	n.a.	n.a.	n.a.	n.a.	n.a.	n.a.
Pyramidal	mouse/rat	351(330)	427 ± 350	5 ± 3	9 ± 4	3.3 ± 2.1	≥ 7.1 ± 3.6	≤ 18 ± 3.0	0.38 ± 0.18	12 ± 13	64 ± 30	≥ 1.0 ± 1.2	1.33	0.26 ± 0.12	≥ 97 ± 173	0.86 ± 0.09
	monkey	867(858)	480 ± 248	6 ± 4	8 ± 3	2.7 ± 1.0	≥ 6.2 ± 3.7	≤ 24 ± 3.9	0.39 ± 0.17	5.7 ± 3.0	99 ± 75	≥ 1.1 ± 1.3	1	0.23 ± 0.09	≥ 65 ± 62	0.89 ± 0.06
	human	1076(1070)	287 ± 95	6 ± 2	7 ± 2	1.9 ± 1.4	≥ 10 ± 3.6	≤ 7.2 ± 5.0	0.27 ± 0.09	5.8 ± 2.4	70 ± 21	≥ 1.5 ± 2.2	0.95	0.29 ± 0.06	≥ 43 ± 21	0.90 ± 0.05
Granule	mouse/rat	128(124)	358 ± 124	2 ± 1	5 ± 2	3.6 ± 1.0	≥ 4.1 ± 0.8	≤ 37 ± 1.9	0.68 ± 0.17	6.7 ± 2.6	109 ± 31	≥ 0.80 ± 0.050	0.51	0.30 ± 0.05	≥ 16 ± 9	0.86 ± 0.04
	monkey	n.a.	n.a.	n.a.	n.a.	n.a.	n.a.	n.a.	n.a.	n.a.	n.a.	n.a.	n.a.	n.a.	n.a.	n.a.
	human	77(77)	538 ± 110	5 ± 1	5 ± 1	2.8 ± 1.0	≥ 5.3 ± 2.7	≤ 77 ± 2.0	0.76 ± 0.38	3.6 ± 0.9	122 ± 27	≥ 1.0 ± 0.2	0.24	0.20 ± 0.04	≥ 17 ± 8	0.84 ± 0.05
Purkinje	mouse/rat	121(120)	158 ± 37	2 ± 1	10 ± 2	1.7 ± 0.49	≥ 7.6 ± 1.3	≤ 24 ± 1.8	0.36 ± 0.07	4.7 ± 2.2	8.6 ± 1.5	≥ 1.2 ± 0.7	0.43	0.27 ± 0.05	≥ 21 ± 9	0.95 ± 0.01
	monkey	n.a.	n.a.	n.a.	n.a.	n.a.	n.a.	n.a.	n.a.	n.a.	n.a.	n.a.	n.a.	n.a.	n.a.	n.a.
	human	n.a.	n.a.	n.a.	n.a.	n.a.	n.a.	n.a.	n.a.	n.a.	n.a.	n.a.	n.a.	n.a.	n.a.	n.a.
Basket	mouse/rat	16(13)	449 ± 242	7 ± 2	10 ± 6	2.5 ± 0.65	≥ 6.3 ± 3.0	≤ 35 ± 3.7	0.43 ± 0.15	15 ± 11	57 ± 36	≥ 1.9 ± 3.8	1.2	0.30 ± 0.12	≥ 11 ± 4	0.88 ± 0.06
	monkey	20(18)	671 ± 302	9 ± 6	19 ± 7	2.5 ± 0.97	≥ 5.9 ± 2.0	≤ 3.7 ± 6.5	0.50 ± 0.18	12 ± 5	64 ± 23	≥ 0.7 ± 0.47	0.31	0.35 ± 0.06	≥ 14 ± 6	0.79 ± 0.06
	human	25(21)	300 ± 344	5 ± 3	7 ± 6	3.2 ± 0.76	≥ 4.75 ± 0.65	≤ 24 ± 2.3	0.60 ± 0.12	7.7 ± 8.9	43 ± 39	≥ 2.6 ± 2.1	0.86	0.24 ± 0.13	≥ 8.2 ± 5.0	0.90 ± 0.08
Gabaergic	mouse/rat	188(157)	284 ± 186	6 ± 2	11 ± 9	1.3 ± 0.29	≥ 7.6 ± 3.4	≤ 24 ± 2.4	0.25 ± 0.05	6.5 ± 2.6	57 ± 38	≥ 4.0 ± 3.1	0.98	30 ± 0.07	≥ 47 ± 61	0.87 ± 0.04
	monkey	n.a.	n.a.	n.a.	n.a.	n.a.	n.a.	n.a.	n.a.	n.a.	n.a.	n.a.	n.a.	n.a.	n.a.	n.a.
	human	8(8)	350 ± 186	6 ± 3	11 ± 4	4.3 ± 0.64	≥ 4.3 ± 0.3	≤ 1.0 ± 0.3	0.65 ± 0.09	13.6 ± 2.7	52 ± 18	≥ 0.59 ± 0.36	1.7	0.36 ± 0.07	≥ 12 ± 3	0.79 ± 0.05
Glutamatergic	mouse/rat	36(35)	756 ± 675	6 ± 2	11 ± 6	1.7 ± 0.38	≥ 8.3 ± 2.6	≤ 6 ± 1.6	0.33 ± 0.05	5.4 ± 1.2	46 ± 17	≥ 1.6 ± 1.2	0.53	0.36 ± 0.06	≥ 16 ± 7	0.85 ± 0.03
	monkey	n.a.	n.a.	n.a.	n.a.	n.a.	n.a.	n.a.	n.a.	n.a.	n.a.	n.a.	n.a.	n.a.	n.a.	n.a.
	human	106(105)	616 ± 111	4 ± 2	6 ± 2	0.84 ± 1.7	≥ 29 ± 10	≤ 0.4 ± 3.3	0.10 ± 0.03	4.0 ± 0.1	145 ± 56	≥ 1.9 ± 1.5	5.8	0.11 ± 0.03	≥ 475 ± 84	0.95 ± 0.02

Table 2: **Summary of the morphological features computed for each species and cell type.** N is the number of cellular structures investigated with complete information about the neurite structure; same information for soma in brackets. The reported values are mean ± s.d. over the corresponding sample. The '≥' and '≤' are used when the estimated value of the corresponding feature may be slightly (on average < 20%) under- or over-estimated, respectively, given the known limitations of the approach used. n.a. = not available.

Morphological Feature	Value Range	Value Mean		
		All Cell Types	Only Neurons	Only Glia
R_{soma} (μm)	$\geq 2 - 29$	≥ 7	≥ 8	≥ 4.0
$\langle R_{branch} \rangle_s$ (μm)	$\geq 0.3 - 4$	≥ 1.6	≥ 1.6	≥ 1.6
CV_{branch}	$0.3 - 5.8$	1.2	1	1
L_{branch} (μm)	$5 - 145$	54	64	11
S/V_{branch} (μm^{-1})	$4 - 16$	8	8	8
$\langle \mu OD_{branch} \rangle_s$	$0.1 - 0.5$	0.3	0.3	0.3
$\langle R_c \rangle_s$ (μm)	$\geq 4 - 475$	≥ 55	≥ 64	≥ 18
τ_{branch}	$0.80 - 0.95$	0.88	0.90	0.92
BO	$4 - 19$	9	9	13
N_{proj}	$2 - 11$	6	5	9
η_{isoma} (%)	$\leq 1 - 86$	≤ 18	≤ 14	≤ 31
R_{domain} (μm)	$40 - 756$	334	400	48

Table 3: **Reference values for all the morphological features of neuronal and glial cells.** The ranges and mean values obtained from the whole dataset investigated are reported, together with mean values for only neurons and glia. The ‘ \geq ’ and ‘ \leq ’ are used when the estimated value of the corresponding feature may be slightly (on average $< 20\%$) under- or over-estimated, respectively, given the known limitations of the approach used.

Cell Type	Species	Shape		
		Watson parameter	Orientation dispersion	Fractional Anisotropy
Microglia	Mouse/Rat	0.99	0.50	0.21 ± 0.11
	Monkey	1.7	0.34	0.21 ± 0.11
	Human	n.a.	n.a.	n.a.
Astrocyte	Mouse/Rat	2.1	0.28	0.34 ± 0.21
	Monkey	n.a.	n.a.	n.a.
	Human	n.a.	n.a.	n.a.
Oligodendrocyte	Mouse/Rat	2.1	0.28	0.24 ± 0.17
	Monkey	n.a.	n.a.	n.a.
	Human	n.a.	n.a.	n.a.
Pyramidal	Mouse/Rat	1.9	0.31	0.33 ± 0.19
	Monkey	2.0	0.30	0.39 ± 0.25
	Human	0.67	0.62	0.45 ± 0.18
Granule	Mouse/Rat	5.8	0.11	0.75 ± 0.16
	Monkey	n.a.	n.a.	n.a.
	Human	3.4	0.18	0.70 ± 0.15
Purkinje	Mouse/Rat	5.3	0.12	0.74 ± 0.08
	Monkey	n.a.	n.a.	n.a.
	Human	n.a.	n.a.	n.a.
Basket	Mouse/Rat	2.1	0.28	0.25 ± 0.19
	Monkey	0.89	0.54	0.39 ± 0.28
	Human	0.98	0.51	0.21 ± 0.21
Gabaergic	Mouse/Rat	1.1	0.47	0.31 ± 0.16
	Monkey	n.a.	n.a.	n.a.
	Human	2.4	0.25	0.25 ± 0.14
Glutamatergic	Mouse/Rat	1.0	0.50	0.24 ± 0.13
	Monkey	n.a.	n.a.	n.a.
	Human	2.7	0.23	0.74 ± 0.04

Table 4: Summary statistics of shape descriptors for each cell type and species. n.a. = not available.

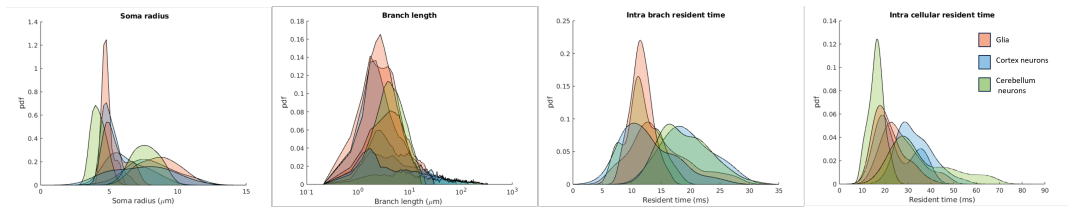


Figure 6: **Probability density functions of soma radius, branch length, intra-branch residence time and intra-cellular residence time for each cell types and all the species.** The residence times were calculated from the surface to volume ratios with a permeability of $20 \mu\text{m}/\text{s}$ [57] and diffusivity typical of water.

3.4 Distribution of some structural features of interest for dMRI modelling

The full distributions of values for some structural features of interest, obtained by merging together all the estimated values from all the species for each cell type, are shown in Fig.6. Given the increasing interest of the microstructure imaging through dMRI community in estimating glia microstructure and the striking difference between the neuronal components of cerebral and cerebellar cortices (e.g., Purkinje cells only in cerebellum), we decided to group them into three classes: glia, cortical neurons and cerebellar neurons, and use three different colors to simplify the visualization of the results.

3.5 Topological distance between cell types

The persistence maps of all the cell types for all species together are shown in Fig.7. These persistence maps are used for each species and each cell type to estimate cell-type specific topological distances, shown in Fig.8.

In rodent cells, there is a notably high global topological distance between glial cells and neurons. This indicates that glial cells exhibit a fundamentally different topological organization compared to neurons. This difference in topology becomes even more evident when considering the comparison along the same length scale. Since glial cells are significantly smaller in size, they inherently display a much smaller topological persistence. This size-related constraint underscores their distinct spatial and structural properties relative to neurons.

Within rodent neurons, granule cells stand out by exhibiting a higher topological distance compared to other neuronal types. This disparity is likely related to their characteristically low branch order, which reflects their simpler dendritic structures and reduced connectivity compared to more complex neurons.

In human cells, however, no significant or consistent trends in topological distance are observed, suggesting greater variability or less pronounced differences in cellular topology among the various cell types.

When examining hominid cells, which include both monkey and human samples, microglia demonstrate a higher topological distance compared to neurons. This observation reinforces the trend seen in rodent cells, further supporting the notion that glial cells, maintain a distinct and conserved topological profile across different species.

In the cross-species comparison between rodent and hominid cells, microglia consistently show a high topological distance relative to neurons, mirroring the trend observed within each species. Additionally, the comparatively low topological distance for microglia across species suggest that their topological properties are consistent, pointing to a shared structural and functional organization in microglia across species.

4 Discussion

4.1 A Quantitative View of Gray Matter Microstructure

GM Intra-Cellular Space. There is currently a lack of in-depth morphological analysis of brain-cell structures of relevance for modelling water diffusion in the GM intra-cellular space. In this work we propose a first analysis with the aim to fill this gap. We estimated a comprehensive set of morphological features useful to GM microstructure modelling from reconstructions of microscopy data from three species. We estimated that neural soma size ranges from 2 to 30 μm in radius with an average of 7 μm and surface-to-volume ratio S/V 0.5 μm^{-1} . Neurons have on average soma twice as big as glial cells, fewer projections radiating from the soma and less projection coverage of soma surface. The radius of cellular projections ranges from 0.3 to 4 μm with average value 1.6 μm and S/V 8 μm^{-1} , similar between neurons and glia. Cellular projections' microscopic orientation dispersion, as defined in [43], is 0.10-0.50, with average value 0.30, similar between neurons and glia; curvature radius is 4-475 μm , with average value of 55 μm . On average, neuronal projections have a curvature radius 6 times larger than glial projections. The branching order of neural cell is 4-20, with average value of 9. Glial cells have branching order 1.5 times larger than neurons. The tortuosity of the branch of neural cell projections is 1.05-1.27, with average value of 1.14, similar between neurons and glial cells. The projections of neural cells extend to distances of 40-756 μm , with neurons on average 400 μm and glial cells on average 50 μm . For completeness, we also report on the relevant features of the GM extra-cellular space and neural cell membrane permeability to water from the literature.

Neural Cell Membrane Permeability to Water. Several works suggest water exchange between unmyelinated neurites and ECS and/or soma occurring on time scales comparable to typical dMRI clinical acquisitions, i.e. 10-100 ms. Although there is not a consensus yet, some works report exchange times t_{ex} for ex vivo mouse brain 5-10 ms [58, 59, 30], suggesting membrane permeability 125 $\mu\text{m/s}$ (like red blood cells), others report t_{ex} for in vivo mouse brain of 20-40 ms [57, 29, 60], suggesting membrane permeability 2-35 $\mu\text{m/s}$. Using

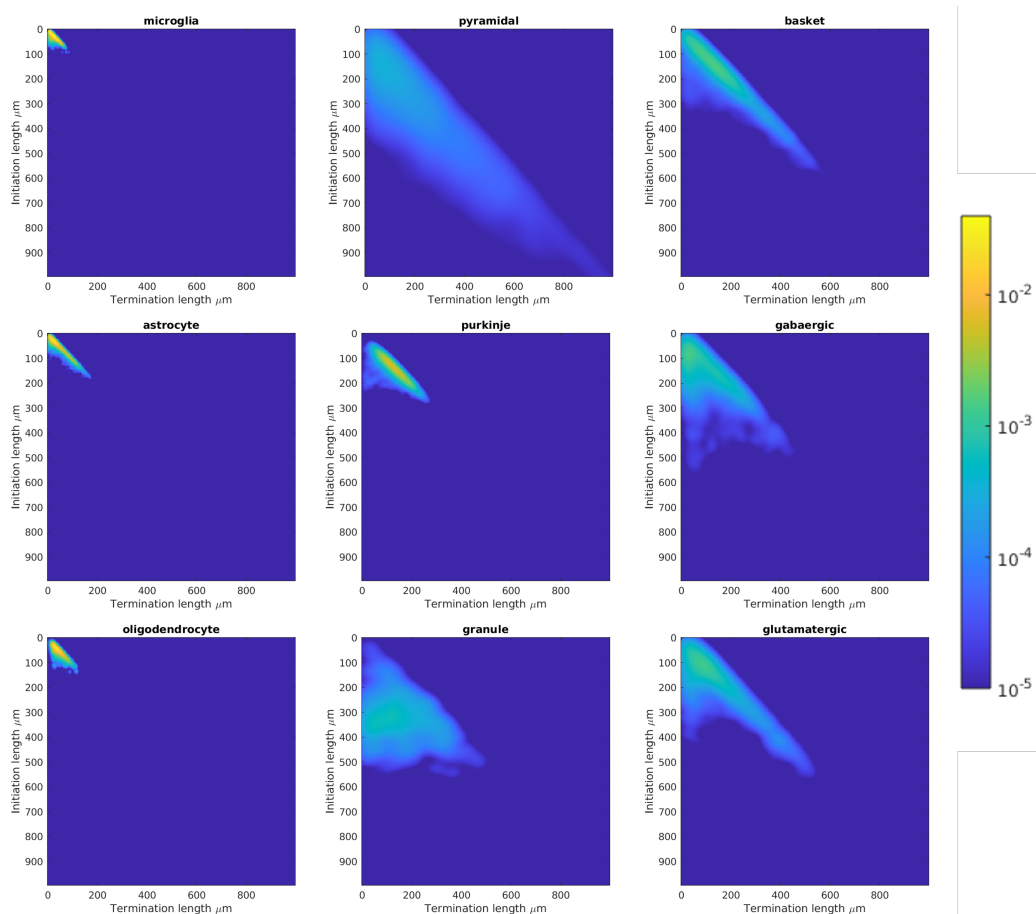


Figure 7: Persistence maps for each cell types and all species together. The persistence map shows at what length scales a given topological feature, here the path length of connected branches, persists. It is computed by tracking the initiation points and termination points, with respect to path length from the soma, of the connected branches at different length scales.

the latter estimates of membrane permeability, and our estimates of the cellular and branch surface-to-volume ratios we estimated distribution of intra-domain and intra-branch residence times that span from a few milliseconds to tens of milliseconds (Fig.6). On average, glial cells have shorter residence times than neurons, and small neurons like granule cells have much shorter residence times than large neurons like pyramidal cells. These observations support the idea of a wide distribution of exchange times within the GM, with water within glial cells in faster exchange with ECS than that within neurons (10-20 ms versus 20-50 ms). We have to acknowledge here that in our analysis we did not include

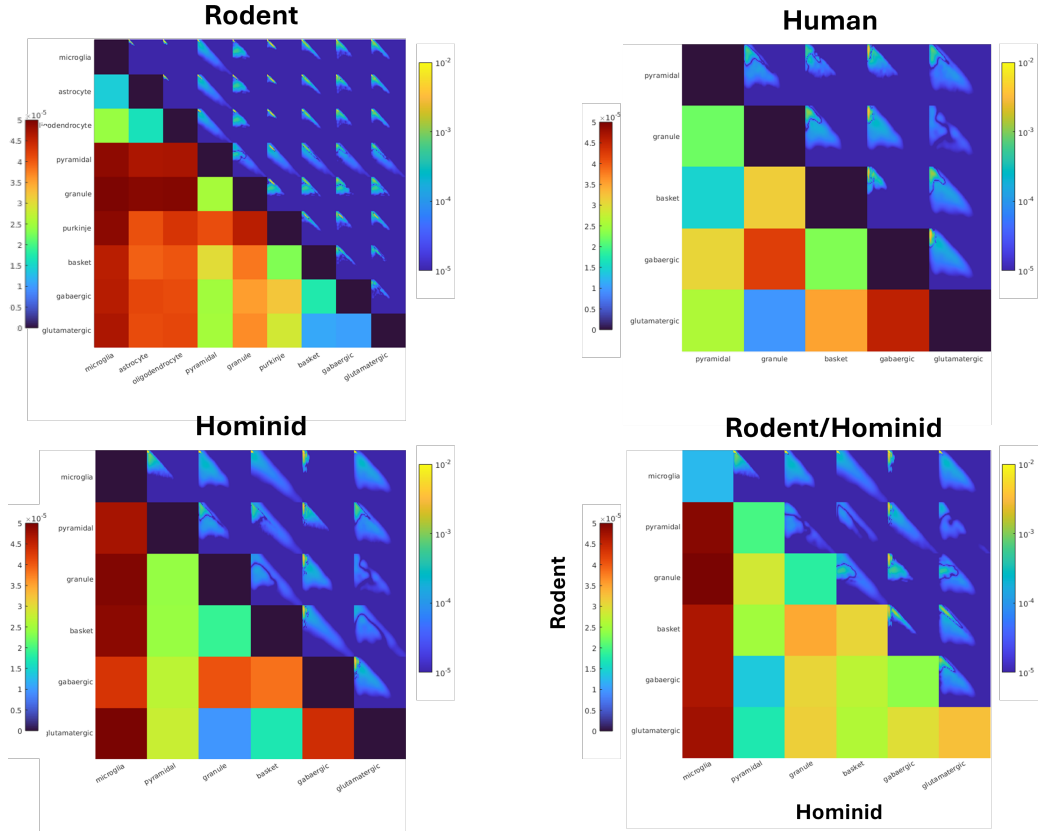


Figure 8: **Local topological distance between images (top right of matrices) and global distance between images (bottom left) for rodent, human, hominid inter species comparison, and a comparison between rodent and hominid cell types**

dendritic spines, boutons and glial lefflets, that can occupy up to 20% of the GM volume [61]. Recent studies have demonstrated that diffusion-mediated exchange between cellular projections' shaft and these small lateral protrusions is another mechanism of water exchange, different from the permeative one, but happening on similar time scales (from a few millisecond to a few tens of milliseconds) [62, 63, 64]. Therefore, the interplay between diffusion-mediated and permeative exchange cannot be neglected when analysing and interpreting time-dependent dMRI measurements in the GM. Appropriate modelling and acquisition strategies to disentangle the two mechanisms and provide unbiased estimates are still missing, and represent an exciting avenue for future research in the field.

4.2 General Implications for Biophysical Modelling

Here we provide a few illustrative examples demonstrating how this study can inform biophysical modelling. Assuming an intra-cellular diffusivity $D=2 \mu m^2/ms$ representative of water and $0.40 \mu m^2/ms$ representative of intracellular brain metabolites, and considering a typical single diffusion encoding acquisition with gradient pulse duration/separation Δ/δ and diffusion time $t_d < 60 ms$, we can infer from Tab.3 that:

- **Soma restriction can be significant for both water and metabolites:** given the low η_{soma} , the soma can significantly restrict diffusion when (from [65]) $5Dt_d \geq R_{soma}^2$, that is for $t_d \geq 5 ms$ for water and $t_d \geq 25 ms$ for metabolites, given a soma radius $R_{soma} \approx 7 \mu m$. This is supported by previous findings which demonstrate the impact of soma contribution on the final dMRI signal [28, 41]
- **Cellular domain restriction is generally negligible for both water and metabolites:** given the size of the cellular domain, it will only significantly restrict molecular diffusion when $5Dt_d \geq R_{domain}^2$, that is for $t_d \geq 160 ms$ for water and $t_d \geq 800 ms$ for metabolites, given $R_{domain} \geq 40 \mu m$, which is far longer than typically used diffusion times t_d .
- **Impact of projections curvedness is generally negligible for both water and metabolites:** the impact of curvedness can only be significant when (from [66]) $2D\Delta, 2D\delta \geq (< R_c >_s)^2$, that is for $\Delta, \delta \geq 750 ms$ for water and $\Delta, \delta \geq 3750 ms$ for metabolites, given $< R_c >_s \approx 55 \mu m$, which is far longer than the values typically. This is further supported by [41].
- **Impact of projection undulation can be significant for both water and metabolites:** the values of $< \mu OD_{branch} >_s$ estimated from the real cellular data match those simulated in [43], from which it can be concluded that undulation can bias the estimation of projection radius in grey matter. However, the average branch radius $< R_{branch} >_s \approx 1.6 \mu m$ is far below the resolution limit of conventional water dMRI techniques [67].
- **Impact of branching is generally negligible for both water and metabolites:** given the branch length $L_{branch} \approx 54 \mu m$, the exchange between branches is negligible for $t_d \ll L_{branch}^2/(2D) \approx 750 ms$ for water and $t_d \ll 3750 ms$ for metabolites, significantly longer than typical t_d used. Further supported by [39, 41].
- **Impact of membrane permeability for cellular projections can be significant for water.** The average intra-branch residence times given the estimated S/V_{branch} are $\approx 20 ms$ for neurons and $\approx 10 ms$ for glial cells. The permeative exchange is thus negligible only for $t_d < 20 ms$ for neuronal projections and for $t_d < 10 ms$ for glial projections; which is not

satisfied in conventional water dMRI applications. Further supported by [29, 41, 60].

- **Impact of projections orientation dispersion can be significant.** Cells with highly oriented and polarized projections, such as Purkinje cells, granule cells and pyramidal neurons have high FA (> 0.50) and low orientation dispersion (< 0.25); while the projections of most of the glial cells and other neuronal cells have low FA (< 0.50) and high orientation dispersion (> 0.25). This supports growing evidence that FA, e.g., from DTI, and orientation dispersion estimates, e.g. from NODDI, can discriminate different cytoarchitectural domains (or layers) in hippocampus, cortex and cerebellum [68, 69, 70, 71, 72].
- **Microglia topology is similar across different species**, suggesting that a single biophysical model of diffusion in microglia would likely hold across species. In contrast, all the other cell-types likely need a dedicated model that accounts for the species-specific topological differences. Exception may be granule cells, that show small differences across species.

4.3 Lessons Learnt for Gray Matter Microstructure Imaging through dMRI

Several attempts to characterize GM microstructure through dMRI have been made in the past [73, 74, 75, 76]. These have focussed on quantifying macro and microscopic anisotropy in the GM, which are dMRI markers informative of the volume fraction and orientation distribution and dispersion of neural cell projections in the tissue. However, GM also contains cell bodies and myelinated and unmyelinated neurites that branch, curve and undulate, alongside a complex and tortuous ECS and permeable cell membranes. Modelling all these features and disentangling their concomitant contributions to the measured dMRI signal is challenging.

In recent years, some steps forward in this direction have been made thanks to the experimental observation that the typical signature of zero radius cylinders (“sticks”) representing the dMRI signal contribution from cellular projections has not been observed in GM at high b values ($> 3ms/\mu m^2$) [77, 26]. This observation stimulated the microstructure imaging community to look for possible explanations, which led to the in-depth investigation of the most likely reasons: (i) neurite curvature [66], branching [38] and/or undulations [30]; (ii) non-negligible signal from water restricted in cell bodies [28]; (iii) non-negligible water exchange across the membrane of cellular projections [29, 30]. All of these can obscure the stick-like signature typical of the dMRI signal from water restricted in cellular projections.

The *hypothesis (i)* has been investigated by Ozarslan et al. [66]. Based on their calculations, the impact of cellular projections’ curvedness on conventional single diffusion encoding acquisitions (e.g., Pulsed Gradient Spin Echo – PGSE) can be significant when $2D\Delta \geq R_c^2$ and $2D\delta \geq R_c^2$, where D is the intracellular

effective water diffusion, Δ/δ the diffusion sensitizing gradient pulses separation/duration and R_c the radius of curvature of cellular projections. Given $D \approx 2.5 \mu\text{m}^2/\text{ms}$ [78] and an average $R_c \approx 55 \mu\text{m}$ [79], this would lead to significant impact of cellular projections' curvedness for $\Delta, \delta \geq 580 \text{ ms}$, which is much longer than the typical timings used in preclinical and clinical applications. Similarly, given projections' branches of average length $\approx 54 \mu\text{m}$ [79], the impact of branching, i.e. exchange between branches, is also likely negligible for diffusion times $< 580 \text{ ms}$. Numerical simulations in microscopy reconstructed neurons [30] also suggest negligible impact of projections' undulations.

The *hypothesis (ii)* is supported experimentally by the agreement between GM data acquired at fixed short diffusion time ($\leq 20 \text{ ms}$) and the soma and neurite density imaging (SANDI) model, which explicitly incorporates a soma compartment [28], and numerically by simulations in computational models of neural cells [80, 28, 39, 30]. It has been shown that SANDI estimates of soma signal fraction in the human cortex mirrors the known cytoarchitectonics of the healthy adult brain [28], and in in vivo mouse brain it strongly correlates with cell density from the Allen Brain Atlas [81]. SANDI also provides estimates of the soma MR apparent radius, but this is expected to overestimate the true radius because of volume weighting and since it is probed indirectly through the diffusivity, which is not linearly dependent on the true radius. Olesen et al. [30] estimated that this overestimation can be up to a factor 1.6 for soma radii matching those of rat pyramidal cells from [79].

The *hypothesis (iii)* is supported experimentally by the agreement between GM data acquired at multiple diffusion times and a modified Kärger's model of two exchanging compartments as in both the neurite exchange imaging (NEXI) model [29] and the standard model with exchange (SMEX) [30]. The analysis of ex vivo rat brain data with SMEX suggests exchange times $t_{ex} \approx 5 \text{ ms}$, close to the $\approx 10 \text{ ms}$ estimated by [58, 59] at 25°C . In contrast, the analysis of in vivo rat brain data with NEXI suggests $t_{ex} \approx 20\text{-}40 \text{ ms}$, longer than the ex vivo case, probably in part due to the fixation process increasing membrane permeability [82]. Nevertheless, there is still no consensus regarding intra-cellular residence time in GM; estimates span values from $\approx 10 \text{ ms}$ to considerably longer than 100 ms [57], perhaps indicating the presence of both fast and slowly exchanging components, as proposed by [83]. The estimated intra-branch and intra-domain residence times we reported (Fig.6) support this hypothesis and the necessity for including exchange between cellular projections and extracellular space for $t_d > 20 \text{ ms}$. However, as discussed in Sec.4.1, the presence of also diffusion-mediated exchange between the cellular projections' shaft and small protrusions on the cellular surface, such as dendritic spines, can confound and bias the estimates of permeative exchange [62, 63, 64], and caution needs to be taken when interpreting time-dependence of dMRI signals in the GM solely due to permeative exchange.

In general, exchange cannot be completely ignored, nor does exchange fully average out the restriction effects of cell membranes, supporting including both neurite exchange and a soma compartment in a parsimonious biophysical model of diffusion in GM, as proposed by Olesen et al. [30] with the SANDIX model.

There are however some caveats to bear in mind when interpreting the model estimates: (a) the soma apparent MR radius is unavoidably an overestimation of the true soma radius; (b) the compartmental signal fractions reflect, apart from volume, also unknown T2 and T1 weighting, which might differ among the compartments; (c) neurite’s fast exchange could be problematic for models based on the Kärger’s model because it could violate the model’s assumptions (i.e. barrier-limited diffusion: $t_{ex} \gg d^2/D$, where d is the neurite diameter; and $\delta \ll t_{ex}$) and lead to biased estimates; (d) molecular diffusion in structural features such as dendritic spines and glial leaflets can lead to diffusion-mediated exchange mechanisms that occur on the same time scales of permeative exchange, making the interpretation of exchange measurements through MRI solely due to permeative exchange fundamentally wrong; (e) using single diffusion encoding acquisitions it is impossible to disentangle restriction and exchange; more refined acquisitions could allow the separation and more accurate quantification of these two effects [59, 84]. The estimates of the model parameters should therefore only be taken as an indication of the true tissue features and validation against realistic numerical simulations and/or alternative measurements in controlled phantoms (e.g. biomimetic tissues and brain organoids) and/or post-mortem samples (e.g., optical, confocal or electron microscopy) remains essential.

4.4 Limitations

Our investigation, while thorough, is not exhaustive (nor could it be). Other features could certainly be measured and tabulated. However, we focus here on those deemed relevant for biophysical modeling in the current literature on microstructure imaging via dMR. We will release our code openly and freely to allow future work to complement this study with additional features and information as needed. Our focus is on a selected set of real three-dimensional reconstructions, as we aim to characterize cellular morphology in the healthy brain. Future studies can use the released code to incorporate more and improved reconstructions of healthy brain tissue as they become available (e.g., through updates to NeuroMorpho or large electron microscopy studies [85, 86]). We provide a few illustrative examples to demonstrate how this study can inform biophysical modeling of dMR signals. However, the information obtained from our investigation has broader applications, and we hope the scientific community will find it valuable for advancing our understanding of gray matter microstructure as a whole. Throughout the manuscript, we discussed the limitations of the morphometric approach used (e.g., an expected underestimation of $< 20\%$ for soma volume and branch radius). Within the constraints of currently available tools, we provide reference values that were previously unavailable. We have taken great care to report error estimates and uncertainties for all measurements to account for these limitations. Future work is needed to improve morphometric algorithms, but this is beyond the scope of the current study.

5 Conclusion

This work provides quantitative information on brain cell structures essential to design sensible biophysical models of the dMRI signal in gray matter. Reporting typical values of relevant features of brain cell morphologies, this study represents a valuable guidebook for the microstructure imaging community and provides illustrative examples demonstrating how to inform biophysical modelling.

Acknowledgments

This work, CAR and MP are supported by the UKRI Future Leaders Fellowship MR/T020296/2.

References

- [1] Constantino Sotelo. Viewing the brain through the master hand of ramón y cajal. *Nature Reviews Neuroscience*, 4(1):71–77, 2003.
- [2] Hongkui Zeng and Joshua R Sanes. Neuronal cell-type classification: challenges, opportunities and the path forward. *Nature Reviews Neuroscience*, 18(9):530–546, 2017.
- [3] Nathan W Gouwens, Staci A Sorensen, Jim Berg, Changkyu Lee, Tim Jarsky, Jonathan Ting, Susan M Sunkin, David Feng, Costas Anastassiou, Eliza Barkan, et al. Classification of electrophysiological and morphological types in mouse visual cortex. *BioRxiv*, page 368456, 2018.
- [4] Linda J Lawson, Victor Hugh Perry, Pietro Dri, and Siamon Gordon. Heterogeneity in the distribution and morphology of microglia in the normal adult mouse brain. *Neuroscience*, 39(1):151–170, 1990.
- [5] Yun-Long Tan, Yi Yuan, and Li Tian. Microglial regional heterogeneity and its role in the brain. *Molecular psychiatry*, 25(2):351–367, 2020.
- [6] Christopher S. Von Bartheld, Jami Bahney, and Suzana Herculano-Houzel. The search for true numbers of neurons and glial cells in the human brain: A review of 150 years of cell counting. *Journal of Comparative Neurology*, 524:3865–3895, December 2016.
- [7] William Bondareff and Joseph J. Pysh. Distribution of the extracellular space during postnatal maturation of rat cerebral cortex. *The Anatomical Record*, 160:773–780, April 1968.
- [8] Muhammad A. Spocter, William D. Hopkins, Sarah K. Barks, Serena Bianchi, Abigail E. Hehmeyer, Sarah M. Anderson, Cheryl D. Stimpson,

- Archibald J. Fobbs, Patrick R. Hof, and Chet C. Sherwood. Neuropil distribution in the cerebral cortex differs between humans and chimpanzees. *Journal of Comparative Neurology*, 520:2917–2929, September 2012.
- [9] Alessandro Motta, Manuel Berning, Kevin M. Boergens, Benedikt Staffler, Marcel Beining, Sahil Loomba, Philipp Hennig, Heiko Wissler, and Moritz Helmstaedter. Dense connectomic reconstruction in layer 4 of the somatosensory cortex. *Science*, 366:eaay3134, November 2019.
- [10] D.P. Pelvig, H. Pakkenberg, A.K. Stark, and B. Pakkenberg. Neocortical glial cell numbers in human brains. *Neurobiology of Aging*, 29:1754–1762, November 2008.
- [11] Lisette Salvesen, Kristian Winge, Tomasz Brudek, Tina Klitmøller Agander, Annemette Løkkegaard, and Bente Pakkenberg. Neocortical Neuronal Loss in Patients with Multiple System Atrophy: A Stereological Study. *Cerebral Cortex*, page bhv228, October 2015.
- [12] Eva Syková and Charles Nicholson. Diffusion in Brain Extracellular Space. *Physiological Reviews*, 88:1277–1340, October 2008.
- [13] Robert G. Thorne and Charles Nicholson. *In Vivo* diffusion analysis with quantum dots and dextrans predicts the width of brain extracellular space. *Proceedings of the National Academy of Sciences*, 103:5567–5572, April 2006.
- [14] Daniel C Alexander, Tim B Dyrby, Markus Nilsson, and Hui Zhang. Imaging brain microstructure with diffusion mri: practicality and applications. *NMR in Biomedicine*, 32(4):e3841, 2019.
- [15] Takuma Mabuchi, Jacinta Lucero, Anne Feng, James A Koziol, and Gregory J Del Zoppo. Focal Cerebral Ischemia Preferentially Affects Neurons Distant from Their Neighboring Microvessels. *Journal of Cerebral Blood Flow & Metabolism*, 25:257–266, February 2005.
- [16] Marijke AM Lemmens, Harry WM Steinbusch, Bart PF Rutten, and Christoph Schmitz. Advanced microscopy techniques for quantitative analysis in neuromorphology and neuropathology research: current status and requirements for the future. *Journal of Chemical Neuroanatomy*, 40(3):199–209, 2010.
- [17] Kevin L Briggman and Davi D Bock. Volume electron microscopy for neuronal circuit reconstruction. *Current opinion in neurobiology*, 22(1):154–161, 2012.
- [18] Jack Reddaway, Peter Eulalio Richardson, Ryan J Bevan, Jessica Stoneman, and Marco Palombo. Microglial morphometric analysis: so many options, so little consistency. *Frontiers in neuroinformatics*, 17:1211188, 2023.

- [19] Ruchi Parekh and Giorgio A Ascoli. Neuronal morphology goes digital: a research hub for cellular and system neuroscience. *Neuron*, 77(6):1017–1038, 2013.
- [20] Eugene Lin and Adam Alessio. What are the basic concepts of temporal, contrast, and spatial resolution in cardiac ct? *Journal of cardiovascular computed tomography*, 3(6):403–408, 2009.
- [21] Ennio Pannese. Morphological changes in nerve cells during normal aging. *Brain Structure and Function*, 216(2):85–89, 2011.
- [22] Denis Le Bihan, Jean-François Mangin, Cyril Poupon, Chris A Clark, Sabina Pappata, Nicolas Molko, and Hughes Chabriat. Diffusion tensor imaging: concepts and applications. *Journal of Magnetic Resonance Imaging: An Official Journal of the International Society for Magnetic Resonance in Medicine*, 13(4):534–546, 2001.
- [23] Hui Zhang, Torben Schneider, Claudia A Wheeler-Kingshott, and Daniel C Alexander. Noddi: practical in vivo neurite orientation dispersion and density imaging of the human brain. *Neuroimage*, 61(4):1000–1016, 2012.
- [24] Els Fieremans, Jens H Jensen, and Joseph A Helpert. White matter characterization with diffusional kurtosis imaging. *Neuroimage*, 58(1):177–188, 2011.
- [25] Daniel C Alexander, Penny L Hubbard, Matt G Hall, Elizabeth A Moore, Maurice Ptito, Geoff JM Parker, and Tim B Dyrby. Orientationally invariant indices of axon diameter and density from diffusion mri. *Neuroimage*, 52(4):1374–1389, 2010.
- [26] Jelle Veraart, Daniel Nunes, Umesh Rudrapatna, Els Fieremans, Derek K Jones, Dmitry S Novikov, and Noam Shemesh. Noninvasive quantification of axon radii using diffusion mri. *elife*, 9:e49855, 2020.
- [27] Yaniv Assaf. Imaging laminar structures in the gray matter with diffusion mri. *Neuroimage*, 197:677–688, 2019.
- [28] Marco Palombo, Andrada Ianus, Michele Guerreri, Daniel Nunes, Daniel C Alexander, Noam Shemesh, and Hui Zhang. Sandi: a compartment-based model for non-invasive apparent soma and neurite imaging by diffusion mri. *Neuroimage*, 215:116835, 2020.
- [29] Ileana O Jelescu, Alexandre de Skowronski, Françoise Geffroy, Marco Palombo, and Dmitry S Novikov. Neurite exchange imaging (nexi): A minimal model of diffusion in gray matter with inter-compartment water exchange. *NeuroImage*, 256:119277, 2022.
- [30] Jonas L Olesen, Leif Østergaard, Noam Shemesh, and Sune N Jespersen. Diffusion time dependence, power-law scaling, and exchange in gray matter. *NeuroImage*, 251:118976, 2022.

- [31] Ileana O Jelescu and Matthew D Budde. Design and validation of diffusion mri models of white matter. *Frontiers in physics*, 5:61, 2017.
- [32] Dmitry S Novikov, Els Fieremans, Sune N Jespersen, and Valerij G Kiselev. Quantifying brain microstructure with diffusion mri: Theory and parameter estimation. *NMR in Biomedicine*, 32(4):e3998, 2019.
- [33] Ileana O Jelescu, Marco Palombo, Francesca Bagnato, and Kurt G Schilling. Challenges for biophysical modeling of microstructure. *Journal of Neuroscience Methods*, 344:108861, 2020.
- [34] Giorgio A Ascoli, Duncan E Donohue, and Maryam Halavi. Neuromorpho.org: a central resource for neuronal morphologies. *Journal of Neuroscience*, 27(35):9247–9251, 2007.
- [35] Hermann Cuntz, Friedrich Forstner, Alexander Borst, and Michael Häusser. The trees toolbox—probing the basis of axonal and dendritic branching, 2011.
- [36] Blender Online Community. *Blender - a 3D modelling and rendering package*. Blender Foundation, Stichting Blender Foundation, Amsterdam, 2018.
- [37] (<https://www.mathworks.com/matlabcentral/fileexchange/5355-toolbox-graph>), MATLAB Central File Exchange. Retrieved July 15, 2024.
- [38] Marco Palombo, Clémence Ligneul, Chloé Najac, Juliette Le Douce, Julien Flament, Carole Escartin, Philippe Hantraye, Emmanuel Brouillet, Gilles Bonvento, and Julien Valette. New paradigm to assess brain cell morphology by diffusion-weighted mr spectroscopy in vivo. *Proceedings of the National Academy of Sciences*, 113(24):6671–6676, 2016.
- [39] Andrada Ianus, Daniel C Alexander, Hui Zhang, and Marco Palombo. Mapping complex cell morphology in the grey matter with double diffusion encoding mr: A simulation study. *Neuroimage*, 241:118424, 2021.
- [40] Mikkel B Hansen, Sune N Jespersen, Lindsey A Leigland, and Christopher D Kroenke. Using diffusion anisotropy to characterize neuronal morphology in gray matter: the orientation distribution of axons and dendrites in the neuromorpho.org database. *Frontiers in integrative neuroscience*, 7:31, 2013.
- [41] Jonas Lynge Olesen and Sune Nørhøj Jespersen. Stick power law scaling in neurons withstands realistic curvature and branching. In *International Society for Magnetic Resonance in Medicine Annual Meeting*, 2020.
- [42] Markus Nilsson, Jimmy Lätt, Freddy Ståhlberg, Danielle van Westen, and Håkan Hagslätt. The importance of axonal undulation in diffusion mr measurements: a monte carlo simulation study. *NMR in Biomedicine*, 25(5):795–805, 2012.

- [43] Jan Brabec, Samo Lasič, and Markus Nilsson. Time-dependent diffusion in undulating thin fibers: Impact on axon diameter estimation. *NMR in Biomedicine*, 33(3):e4187, 2020.
- [44] Dmitry S Novikov and Valerij G Kiselev. Surface-to-volume ratio with oscillating gradients. *Journal of magnetic resonance*, 210(1):141–145, 2011.
- [45] Hong-Hsi Lee, Antonios Papaioannou, Sung-Lyoung Kim, Dmitry S Novikov, and Els Fieremans. A time-dependent diffusion mri signature of axon caliber variations and beading. *Communications biology*, 3(1):354, 2020.
- [46] Dmitry S Novikov, Jens H Jensen, Joseph A Helpert, and Els Fieremans. Revealing mesoscopic structural universality with diffusion. *Proceedings of the National Academy of Sciences*, 111(14):5088–5093, 2014.
- [47] Marco Palombo, Daniel C Alexander, and Hui Zhang. A generative model of realistic brain cells with application to numerical simulation of the diffusion-weighted mr signal. *NeuroImage*, 188:391–402, 2019.
- [48] Sergio Luengo-Sanchez, Concha Bielza, Ruth Benavides-Piccione, Isabel Fernaud-Espinosa, Javier DeFelipe, and Pedro Larrañaga. A univocal definition of the neuronal soma morphology using gaussian mixture models. *Frontiers in neuroanatomy*, 9:137, 2015.
- [49] Marwan Abdellah, Juan Hernando, Stefan Eilemann, Samuel Lapere, Nicolas Antille, Henry Markram, and Felix Schürmann. Neuromorphovis: a collaborative framework for analysis and visualization of neuronal morphology skeletons reconstructed from microscopy stacks. *Bioinformatics*, 34(13):i574–i582, 2018.
- [50] Marwan Abdellah, Juan José García Cantero, Nadir Román Guerrero, Alessandro Foni, Jay S Coggan, Corrado Calì, Marco Agus, Eleftherios Zisis, Daniel Keller, Markus Hadwiger, et al. Ultraliser: a framework for creating multiscale, high-fidelity and geometrically realistic 3d models for in silico neuroscience. *Briefings in bioinformatics*, 24(1):bbac491, 2023.
- [51] Dmitry S Novikov, Jelle Veraart, Ileana O Jelescu, and Els Fieremans. Rotationally-invariant mapping of scalar and orientational metrics of neuronal microstructure with diffusion mri. *NeuroImage*, 174:518–538, 2018.
- [52] Kanti V Mardia and Peter E Jupp. *Directional statistics*. John Wiley & Sons, 2009.
- [53] Gerhard Kurz, Igor Gilitschenski, Florian Pfaff, Lukas Drude, Uwe D. Hanebeck, Reinhold Haeb-Umbach, and Roland Y. Siegwart. Directional statistics and filtering using libDirectional. *Journal of Statistical Software*, 89(4):1–31, 2019.

- [54] Lida Kanari, Paweł Dłotko, Martina Scolamiero, Ran Levi, Julian Shillcock, Kathryn Hess, and Henry Markram. A topological representation of branching neuronal morphologies. *Neuroinformatics*, 16:3–13, 2018.
- [55] Lida Kanari, Hugo Dictus, Athanassia Chalimourda, Alexis Arnaudon, Werner Van Geit, Benoit Coste, Julian Shillcock, Kathryn Hess, and Henry Markram. Computational synthesis of cortical dendritic morphologies. *Cell Reports*, 39(1), 2022.
- [56] Lida Kanari, Adélie Garin, and Kathryn Hess. From trees to barcodes and back again: theoretical and statistical perspectives. *Algorithms*, 13(12):335, 2020.
- [57] Donghan M. Yang, James E. Huettner, G. Larry Bretthorst, Jeffrey J. Neil, Joel R. Garbow, and Joseph J.H. Ackerman. Intracellular water preexchange lifetime in neurons and astrocytes. *Magnetic Resonance in Medicine*, 79:1616–1627, March 2018.
- [58] Nathan H Williamson, Rea Ravin, Dan Benjamini, Hellmut Merkle, Melanie Falgairolle, Michael James O’Donovan, Dvir Blivis, Dave Ide, Teddy X Cai, Nima S Ghorashi, Ruiliang Bai, and Peter J Basser. Magnetic resonance measurements of cellular and sub-cellular membrane structures in live and fixed neural tissue. *eLife*, 8:e51101, December 2019.
- [59] Teddy X. Cai, Nathan H. Williamson, Rea Ravin, and Peter J. Basser. Disentangling the Effects of Restriction and Exchange With Diffusion Exchange Spectroscopy. *Frontiers in Physics*, 10:805793, March 2022.
- [60] Eloïse Mougél, Julien Valette, and Marco Palombo. Investigating exchange, structural disorder, and restriction in gray matter via water and metabolites diffusivity and kurtosis time-dependence. *Imaging Neuroscience*, 2:1–14, 04 2024.
- [61] Narayanan Kasthuri, Kenneth Jeffrey Hayworth, Daniel Raimund Berger, Richard Lee Schalek, José Angel Conchello, Seymour Knowles-Barley, Dongil Lee, Amelio Vázquez-Reina, Verena Kaynig, Thouis Raymond Jones, Mike Roberts, Josh Lyskowski Morgan, Juan Carlos Tapia, H. Sebastian Seung, William Gray Roncal, Joshua Tzvi Vogelstein, Randal Burns, Daniel Lewis Sussman, Carey Eldin Priebe, Hanspeter Pfister, and Jeff William Lichtman. Saturated reconstruction of a volume of neocortex. *Cell*, 162(3):648–661, 2015.
- [62] Marco Palombo, Clemence Ligneul, Edwin Hernandez-Garzon, and Julien Valette. Can we detect the effect of spines and leaflets on the diffusion of brain intracellular metabolites? *NeuroImage*, 182:283–293, 2018.
- [63] Kadir Şimşek and Marco Palombo. Diffusion in dendritic spines: impact on permeative exchange estimation with time-dependent diffusion-weighted mri. *Proc. Intl. Soc. Mag. Reson. Med. 2024.*, 3456, 2024.

- [64] Arthur Chakwizira, Kadir Şimşek, Marco Palombo, Filip Szczepankiewicz, Linda Knutsson, and Markus Nilsson. Water exchange as measured by diffusion mri with free gradient waveforms: A potential biomarker of dendritic spine morphology. *Proc. Intl. Soc. Mag. Reson. Med.* 2024., 3463, 2024.
- [65] Paul T Callaghan. *Principles of nuclear magnetic resonance microscopy*. Clarendon press, 1993.
- [66] Evren Özarslan, Cem Yolcu, Magnus Herberthson, Hans Knutsson, and Carl-Fredrik Westin. Influence of the size and curvedness of neural projections on the orientationally averaged diffusion mr signal. *Frontiers in physics*, 6:17, 2018.
- [67] Markus Nilsson, Samo Lasič, Ivana Drobnjak, Daniel Topgaard, and Carl-Fredrik Westin. Resolution limit of cylinder diameter estimation by diffusion mri: The impact of gradient waveform and orientation dispersion. *NMR in Biomedicine*, 30(7):e3711, 2017.
- [68] Nian Wang, Jieying Zhang, Gary Cofer, Yi Qi, Robert J. Anderson, Leonard E. White, and G. Allan Johnson. Neurite orientation dispersion and density imaging of mouse brain microstructure. *Brain Structure and Function*, 224:1797–1813, 2019.
- [69] Nian Wang, Leonard E. White, Yi Qi, Gary Cofer, and G. Allan Johnson. Cytoarchitecture of the mouse brain by high resolution diffusion magnetic resonance imaging. *NeuroImage*, 216:116876, 2020.
- [70] G. Allan Johnson, Yuqi Tian, David G. Ashbrook, Gary P. Cofer, James J. Cook, James C. Gee, Adam Hall, Kathryn Hornburg, Catherine C. Kaczorowski, Yi Qi, Fang-Cheng Yeh, Nian Wang, Leonard E. White, and Robert W. Williams. Merged magnetic resonance and light sheet microscopy of the whole mouse brain. *Proceedings of the National Academy of Sciences*, 120(17):e2218617120, 2023.
- [71] Nian Wang, Surendra Maharjan, Andy P. Tsai, Peter B. Lin, Yi Qi, Abigail Wallace, Megan Jewett, Fang Liu, Gary E. Landreth, and Adrian L. Oblak. Integrating multimodality magnetic resonance imaging to the allen mouse brain common coordinate framework. *NMR in Biomedicine*, 36(5):e4887, 2023.
- [72] Xinyue Han, Surendra Maharjan, Jie Chen, Yi Zhao, Yi Qi, Leonard E. White, G. Allan Johnson, and Nian Wang. High-resolution diffusion magnetic resonance imaging and spatial-transcriptomic in developing mouse brain. *NeuroImage*, 297:120734, 2024.
- [73] Sune N Jespersen, Christopher D Kroenke, Leif Østergaard, Joseph JH Ackerman, and Dmitriy A Yablonskiy. Modeling dendrite density from magnetic resonance diffusion measurements. *Neuroimage*, 34(4):1473–1486, 2007.

- [74] M.E. Komlosh, F. Horkay, R.Z. Freidlin, U. Nevo, Y. Assaf, and P.J. Basser. Detection of microscopic anisotropy in gray matter and in a novel tissue phantom using double Pulsed Gradient Spin Echo MR. *Journal of Magnetic Resonance*, 189:38–45, November 2007.
- [75] Noam Shemesh, Evren Özarlan, Peter J. Basser, and Yoram Cohen. Accurate noninvasive measurement of cell size and compartment shape anisotropy in yeast cells using double-pulsed field gradient MR. *NMR in Biomedicine*, 25:236–246, February 2012.
- [76] Trong-Kha Truong, Arnaud Guidon, and Allen W. Song. Cortical Depth Dependence of the Diffusion Anisotropy in the Human Cortical Gray Matter In Vivo. *PLoS ONE*, 9:e91424, March 2014.
- [77] Emilie T. McKinnon, Jens H. Jensen, G. Russell Glenn, and Joseph A. Helpert. Dependence on b-value of the direction-averaged diffusion-weighted imaging signal in brain. *Magnetic Resonance Imaging*, 36:121–127, February 2017.
- [78] Bibek Dhital, Marco Reisert, Elias Kellner, and Valerij G. Kiselev. Intra-axonal diffusivity in brain white matter. *NeuroImage*, 189:543–550, April 2019.
- [79] Marco Palombo, Daniel C Alexander, and Hui Zhang. Large-scale analysis of brain cell morphometry informs microstructure modelling of gray matter. In *Proc. Intl. Soc. Mag. Reson. Med.*, volume 29, 2021.
- [80] Chengran Fang, Van-Dang Nguyen, Demian Wassermann, and Jing-Rebecca Li. Diffusion MRI simulation of realistic neurons with SpinDoctor and the Neuron Module. *NeuroImage*, 222:117198, November 2020.
- [81] Andrada Ianuş, Joana Carvalho, Francisca F. Fernandes, Renata Cruz, Cristina Chavarrias, Marco Palombo, and Noam Shemesh. Soma and Neurite Density MRI (SANDI) of the in-vivo mouse brain and comparison with the Allen Brain Atlas. *NeuroImage*, 254:119135, July 2022.
- [82] Timothy M. Shepherd, Jeremy J. Flint, Peter E. Thelwall, Greg J. Stanisz, Thomas H. Mareci, Anthony T. Yachnis, and Stephen J. Blackband. Post-mortem interval alters the water relaxation and diffusion properties of rat nervous tissue — Implications for MRI studies of human autopsy samples. *NeuroImage*, 44:820–826, February 2009.
- [83] Markus Nilsson, Jimmy Lätt, Danielle Van Westen, Sara Brockstedt, Samo Lasič, Freddy Ståhlberg, and Daniel Topgaard. Noninvasive mapping of water diffusional exchange in the human brain using filter-exchange imaging. *Magnetic Resonance in Medicine*, 69:1572–1580, June 2013.
- [84] Arthur Chakwizira, Carl-Fredrik Westin, Jan Brabec, Samo Lasič, Linda Knutsson, Filip Szczepankiewicz, and Markus Nilsson. Diffusion MRI with

pulsed and free gradient waveforms: Effects of restricted diffusion and exchange. *NMR in Biomedicine*, 36:e4827, January 2023.

- [85] Nicholas L. Turner, Thomas Macrina, J. Alexander Bae, Runzhe Yang, Alyssa M. Wilson, Casey Schneider-Mizell, Kisuk Lee, Ran Lu, Jingpeng Wu, Agnes L. Bodor, Adam A. Bleckert, Derrick Brittain, Emmanouil Froudarakis, Sven Dorkenwald, Forrest Collman, Nico Kemnitz, Dodam Ih, William M. Silversmith, Jonathan Zung, Aleksandar Zlateski, Ignacio Tartavull, Szi-chieh Yu, Sergiy Popovych, Shang Mu, William Wong, Chris S. Jordan, Manuel Castro, JoAnn Buchanan, Daniel J. Bumbarger, Marc Takeno, Russel Torres, Gayathri Mahalingam, Leila Elabbady, Yang Li, Erick Cobos, Pengcheng Zhou, Shelby Suckow, Lynne Becker, Liam Paninski, Franck Polleux, Jacob Reimer, Andreas S. Tolias, R. Clay Reid, Nuno Maçarico da Costa, and H. Sebastian Seung. Reconstruction of neocortex: Organelles, compartments, cells, circuits, and activity. *Cell*, 185(6):1082–1100.e24, Mar 2022.
- [86] Alexander Shapson-Coe, Michał Januszewski, Daniel R. Berger, Art Pope, Yuelong Wu, Tim Blakely, Richard L. Schalek, Peter H. Li, Shuohong Wang, Jeremy Maitin-Shepard, Neha Karlupia, Sven Dorkenwald, Evelina Sjostedt, Laramie Leavitt, Dongil Lee, Jakob Troidl, Forrest Collman, Luke Bailey, Angerica Fitzmaurice, Rohin Kar, Benjamin Field, Hank Wu, Julian Wagner-Carena, David Aley, Joanna Lau, Zudi Lin, Donglai Wei, Hanspeter Pfister, Adi Peleg, Viren Jain, and Jeff W. Lichtman. A petavoxel fragment of human cerebral cortex reconstructed at nanoscale resolution. *Science*, 384(6696):eadk4858, 2024.